

INFLUENCE OF SKIN CURVATURE ON WINGBOX OPTIMIZATION WITH NONLINEAR STRUCTURAL STABILITY CONSTRAINTS

Francesco M. A. Mitrotta¹, Alberto Pirrera¹, Terence Macquart¹, Jonathan E. Cooper¹, Alex Pereira do Prado² & Pedro Higino Cabral²

¹University of Bristol, Queen's Building, University Walk, Bristol BS8 1TR, UK ²Embraer S.A., São José dos Campos, São Paulo, 12227-901, Brazil

Abstract

This paper investigates the influence of skin curvature on the nonlinear structural stability response and optimization of wingbox structures. The study compares the optimization of two idealized versions of the Common Research Model wingbox, called the CRM-like box beam, employing curved and flat skin, and enforcing linear and nonlinear structural stability constraints. The findings demonstrate that for the nonlinear structural stability approach the flat skin model provides non-conservative estimates of critical stability loads, leading to over-optimistic mass reductions. Therefore, accurate modeling of skin curvature is essential for reliable structural stability assessments and optimization outcomes. The results underline the importance of incorporating realistic skin curvatures in future aeroelastic optimization frameworks employing nonlinear structural stability constraints.

Keywords: Aeroelastic optimization, nonlinear structural stability, wingbox, skin curvature, buckling

1. Introduction

In 2021, the Air Transport Action Group set an ambitious goal for global civil aviation to achieve net-zero carbon emissions by 2050 [1], in line with the Paris Agreement's aim to limit global warming to below $1.5\,^{\circ}$ C. This objective poses a significant challenge for the aviation industry, necessitating innovative approaches to aircraft design.

The push towards net-zero aviation has intensified the focus on developing fuel-efficient aircraft. According to the Breguet Range equation, emission reductions can be achieved through lighter aircraft, improved aerodynamics, and enhanced engine efficiency [2]. Recent decades have seen substantial advancements in aeroelastic optimization tools for designing lightweight structures, primarily driven by the integration of composite materials, which offer high specific strength and stiffness, along with extensive elastic tailoring capabilities.

In aeroelastic optimizations, static structural stability often emerges as a critical constraint [3, 4, 5, 6, 7, 8, 9, 10, 11, 12, 13, 14, 15]. Typically, linear buckling analyses are used to impose this constraint, involving eigenvalue problems based on the linearization of the structural response around the undeformed configuration. While computationally efficient and straightforward to implement, these analyses tend to over-constrain the design space, potentially leading to over-designed structures. In fact, in advanced design stages, aerospace structures are sized to bear loads beyond their linear buckling point [16].

In a recent study [17], we proposed the hypothesis that, in current aeroelastic optimizations, linear buckling evaluations place a glass ceiling on the sizing loads that the wing structure is designed for, curtailing in this way the maximum load-carrying capacity. This limitation is particularly relevant for evolving wing designs driven by sustainability goals, where the increasing slenderness and compliance of wings make nonlinear effects more significant. Consequently, we argue that nonlinear evaluations of structural stability could lead to more efficient design solutions.

In the same study, we introduced a novel nonlinear structural stability constraint for optimizing wingbox structures [17]. This approach involved enforcing the positive-definiteness of the tangent stiffness matrix by monitoring its smallest magnitude eigenvalues throughout the nonlinear analysis and ensuring they remain positive.

We validated this concept through a structural optimization of an idealized model of the Common Research Model (CRM) [18] wingbox, referred to as the CRM-like box beam, using a concentrated tip load and uniform wall thickness. The optimization with nonlinear structural stability constraints resulted in an 11% mass reduction compared to a baseline structure optimal in linear buckling terms. In a more recent study [19], we increased the realism of the optimization scenario by using a linearly varying thickness along the model's length and a distributed load, achieving mass reductions of up to 9% compared to the linearly optimized structure.

Building on our previous work, this paper applies the nonlinear structural stability constraint to the CRM-like box beam model with curved skin and compares the optimization results with those of a model employing flat skin. In fact, beyond the use of linear methods, aeroelastic optimization frameworks typically assume the skin panels to be flat. This assumption is conservative, as the linear buckling load of a flat panel is lower than that of a curved panel. This additional conservatism exacerbates the glass ceiling imposed by linear buckling, further hindering the exploitation of the structure's full load-carrying capacity. Although curvature is known to significantly affect the nonlinear stability response of thin-walled structures, the impact of skin curvature within the context of nonlinear structural stability constraints for optimizing wingbox structures remains an open question.

The remainder of the paper is structured as follows: Section 2. provides the theoretical background on the nonlinear structural stability constraint. Section 3. presents the numerical model and the definition of the optimization problems. Finally, Section 4. investigates the influence of skin curvature on both the initial and optimized structures.

The results of this study can be reproduced through open-source Jupyter notebooks available in a GitHub repository¹, where additional resources on this research are also available.

2. Nonlinear Structural Stability Constraint

2.1 Stability assessment

To calculate equilibrium points and assess their stability in the geometrically nonlinear analysis of structures under conservative loads, it is necessary to consider the total potential energy, Π , which is given by the difference between the internal strain energy, U, and the external work done [20], W, i.e.

$$\Pi = U - W. \tag{1}$$

In general, the total potential energy is a function of the state parameters, \mathbf{u} , corresponding to the structural degrees of freedom, and other parameters such as the applied loads, \mathbf{p} , whence $\Pi = \Pi(\mathbf{u}, \mathbf{p})$.

Equilibrium is found at points where the total potential energy has a stationary value, or in other words where its first derivative with respect to the states is zero, such that

$$\frac{\partial \Pi}{\partial u} = \mathbf{0}.\tag{2}$$

The stability of the equilibrium points depends on the second derivative of the potential energy with respect to the state parameters. This means that we need to consider the Hessian of the potential energy, which corresponds to the tangent stiffness matrix, so

$$\frac{\partial^2 \Pi}{\partial \boldsymbol{u}^2} = \boldsymbol{H}_{\Pi} = \boldsymbol{K}_T. \tag{3}$$

The tangent stiffness matrix represents the local, point-wise tangent to the load-displacement manifold and changes at every equilibrium point found during the nonlinear analysis. The stability of an

¹https://github.com/fmamitrotta/nonlinear-structural-stability-notebooks, accessed May 2024.

equilibrium point is thus established as

$$\textit{\textbf{K}}_{T}(\textit{\textbf{u}}) \left\{ egin{array}{ll} ext{positive definite} \Rightarrow ext{stable equilibrium;} \\ ext{singular} \Rightarrow ext{neutral equilibrium;} \\ ext{indefinite or negative definite} \Rightarrow ext{unstable equilibrium.} \end{array} \right. \tag{4}$$

In the context of an aircraft wing, it is desirable that the structure is always loaded along a stable equilibrium path. Traversing unstable equilibria may indeed cause sudden snap-throughs, which, be it local or global, may cause structural damage. For this reason, the nonlinear structural stability constraint employed here consists in enforcing the tangent stiffness matrix to be positive definite for all converged increments of the nonlinear analysis, or in other words, for all the calculated equilibrium points.

The definiteness of a matrix can be evaluated by considering its eigenvalues. Consequently, we can recast Eq. (4) as

$$\textit{\textbf{K}}_{T}(\textit{\textbf{u}}) \left\{ egin{array}{l} \text{all eigenvalues} > 0 \Rightarrow \text{stable equilibrium;} \\ \text{at least one eigenvalue} = 0 \Rightarrow \text{neutral equilibrium;} \\ \text{at least one eigenvalue} < 0 \Rightarrow \text{unstable equilibrium}^{2}. \end{array} \right.$$

Equation (5) means that we can evaluate the nonlinear structural stability of the structure by monitoring the eigenvalues, λ , of the tangent stiffness matrix for each converged increment of the nonlinear analysis. However, the size of the tangent stiffness matrix of typical Finite Element (FE) models employed in aeroelastic optimizations makes the computation of all eigenvalues impractical. For this reason, only the N_{λ} smallest magnitude eigenvalues are monitored, and they are constrained to remain positive.

2.2 Nonlinear solver

The way in which a structure's equilibrium path is traced depends on the method employed to solve the nonlinear governing equilibrium equation. Herein, we focus on static analyses with conservative loads and we require the nonlinear solver to be able to follow both stable and unstable paths to provide a robust approach for the evaluation of the nonlinear stability constraint function.

The nonlinear equilibrium equations of a structure can be expressed as a force balance between internal and conservative external forces

$$R(\mathbf{u}, \mu) = f(\mathbf{u}) - p(\mu) = f(\mathbf{u}) - \mu \hat{\mathbf{p}} = \mathbf{0}$$
(6)

where ${\it R}$ is a residual, ${\it u}$ is the displacement vector, ${\it \mu}$ a scalar loading parameter, ${\it f}$ the vector of internal forces, which is only dependent on ${\it u}$, and ${\it p}$ the vector of conservative external forces. The latter expression can be refactored in terms of a force vector ${\it \hat{p}}$ multiplied by the loading parameter ${\it \mu}$, independent of the displacements, as in nonlinear problems the external loads are usually applied in increments.

The aeroelastic optimization frameworks that feature nonlinear structural analysis, typically employ load control methods to solve Eq. (6) [12, 15]. With this approach, a load value is imposed at every consecutive increment of the nonlinear analysis and held constant during Newton-Raphson iterations until convergence is achieved. Upon convergence, the analysis moves on to the next load increment. This method has issues with load limit point bifurcations, because it cannot follow the unstable segment of the equilibrium path beyond the limit point, where the applied load decreases. In fact, the solver might jump to the next available equilibrium point for the new increment above the limit point, or it might not achieve convergence at all [21]. In both cases load controlled increments cannot find unstable equilibrium points, making them unsuitable for an aeroelastic optimization framework that aims

²In the case of at least one zero and one negative eigenvalue occurring simultaneously, the equilibrium is neutral along the principal stiffness directions associated with the zero eigenvalues and unstable along the principal stiffness directions associated with the negative eigenvalues. Consequently, the structure is considered unstable overall.

to evaluate structural stability with nonlinear methods. Similar problems are faced by displacement-controlled solutions, but at displacement limit points.

Considering the above requirements, the chosen strategy for the solution of Eq. (6) is path-following with arc-length control. In this approach, the solution path is traced with an incremental-iterative method that imposes a simultaneous variation of load and displacement variables for the solution of the linearized equilibrium equations. The i^{th} equilibrium point is searched at an arc-length distance Δs^i from the last known equilibrium, Δs^i being calculated via a norm of the increment $(\Delta \mathbf{u}^i, \Delta \mu^i)$. The iterations are constrained to lie on the surface created by the arc, and they eventually converge at the intersection of the arc and the equilibrium path. In this way, arc-length methods can successfully calculate the equilibrium path of a structure also in presence of instabilities like limit point bifurcations [21]. Consequently, the arc-length method is chosen for the evaluation of the nonlinear structural stability constraint employed in this paper, as it can successfully follow stable as well unstable segments of an equilibrium path.

3. Definition of the structural model and of the optimization problems

In this section, we define the numerical model of the CRM-like box beam, the design load used for the optimizations discussed in Section 4, and the optimization problems with linear buckling and nonlinear structural stability constraints.

3.1 The CRM-like box beam model

The CRM-like box beam is a straight box beam idealization of the CRM wingbox based on the data provided in [22]. It was developed for a previous study [17], where its sizing is reported, to obtain a relatively simple representation of a typical wingbox structure used in aeroelastic optimizations. To investigate the nonlinear structural stability response, the model was developed to retain only the essential features that influence such a response, that is to say ribs and skin stiffeners. Specifically, the CRM-like box beam is reinforced by 19 equally spaced ribs and 2 equally spaced stiffeners on each skin. The model's geometry and dimensions are depicted in Fig. 1, while the cross-sectional and material properties of the model are summarized in Table 1.

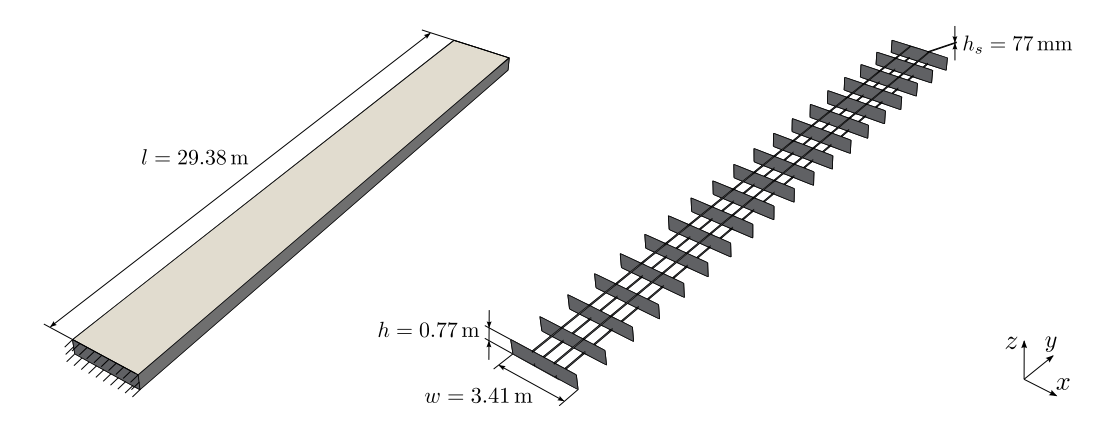


Figure 1 – Geometry and dimensions of the CRM-like box beam model.

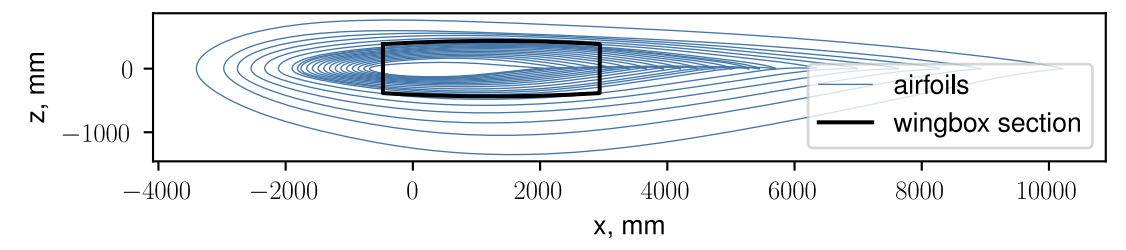
Table 1 – CRM-like box beam cross-sectional and material properties. Material properties from [23]. The same thickness is used for all structural parts: skin, spars, ribs and stiffeners.

Parameter	Value	
Wall thickness	7.7 mm	
Density	2780 kg/m ³	
Young's modulus	$73.1 \cdot 10^9 \text{ Pa}$	
Poisson's ratio	0.3	
Yield strength	420 · 10 ⁶ Pa	

Here, we present a variation of the CRM-like box beam employing curved skin. To maintain the simplicity of our approach, we model the profile of the top and bottom skin as two symmetric shallow cylindrical arches. Consequently, the curvature of the two skin can be uniquely defined by the maximum height of the arch.

To find a value of maximum arch height that results in a realistic skin curvature, we consider the CRM airfoils data provided in [22], plot the airfoils with zero twist, aligned at the quarter-chord location, and superimpose the section of the CRM-like box beam. In this way, several maximum arch heights can be tested and the best match with the airfoil curvature can be found. The best match between the upper profile of the CRM-like box beam section and the upper surface of the closest CRM airfoil is obtained for a maximum arch height equal to h/15, as it can be observed in Fig. 2. This value is thus used in the remainder of the paper for the model with curved skin.

As expected, and as observed in Fig. 2b, it is not possible to obtain a close match with both the upper and lower surface of the CRM airfoil by modelling the two skin as symmetric arches. In fact, the CRM airfoils are supercritical airfoils, meaning that they employ a flatter upper surface and a more curved lower surface to obtain favorable aerodynamic characteristic in the transonic flow regime typical of commercial aircraft. Here, we focus on obtaining a good match with the upper surface of the airfoil because the top skin is the structural part that undergoes compression for the load case taken into consideration.



(a) Overview of CRM airfoils and CRM-like box beam section.

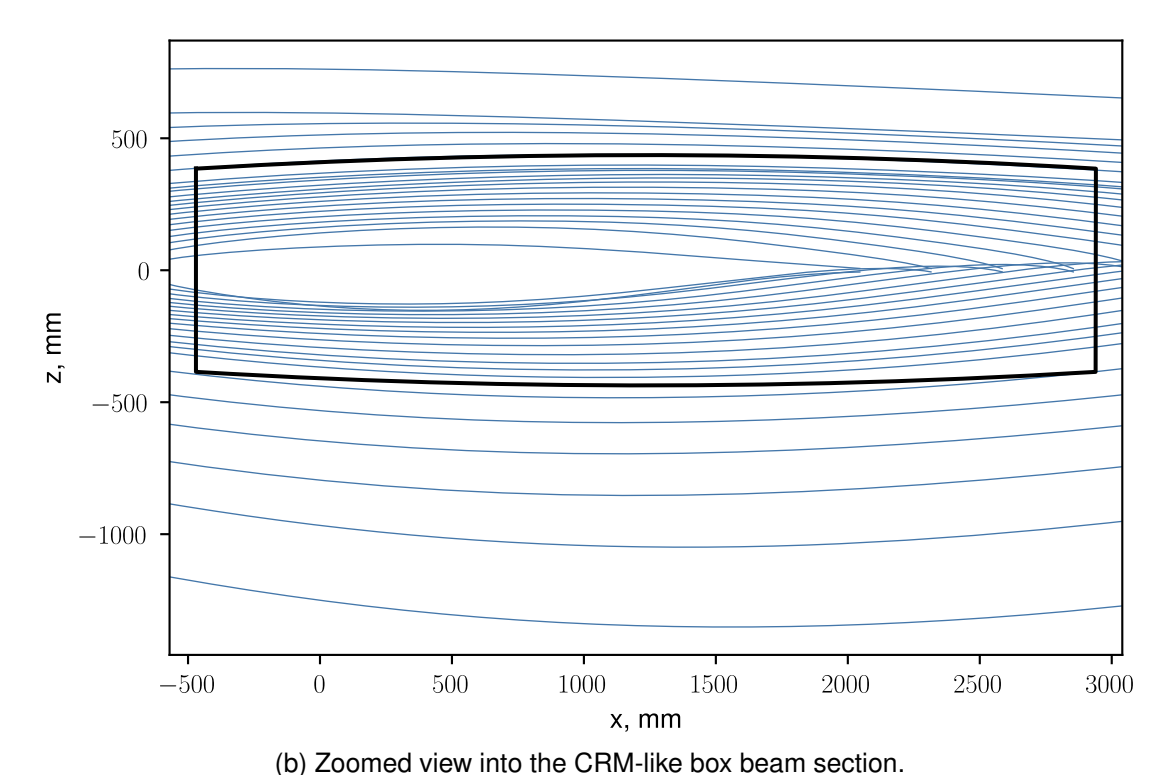


Figure 2 – CRM airfoils and CRM-like box beam section.

The numerical model is implemented in MSC Nastran, where all geometrical parts are discretized using CQUAD4 (thin shell) elements. Fixed boundary conditions are enforced at the root section by means of a SPC1 card.

3.2 Optimization problems

Both the flat and the curved skin models are optimized through two subsequent mass-minimization problems: one defined with linear buckling constraints and the other defined with nonlinear structural stability constraints. We use the same design load for all optimizations, choosing an elliptical load distribution over the length of the structure to loosely mimic an aerodynamic load. This load is split between the top and the bottom skin and it is introduced by means of nodal non-follower forces defined at every node of the two skin, as illustrated in Fig. 3. The overall magnitude of the design load is chosen to be equal to the linear buckling load obtained for the model with curved skin.

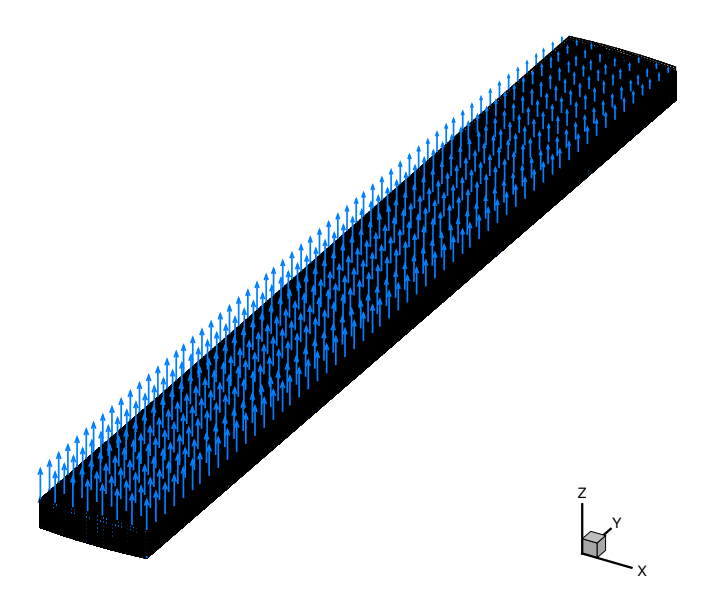


Figure 3 – Elliptical load distribution applied to the CRM-like box beam. Force vectors are sub-sampled for clarity.

A mesh convergence study was conducted on the model with curved skin to determine an appropriate mesh size that balances computational efficiency with accuracy. The final converged mesh consists of approximately $3.3 \cdot 10^4$ elements and results in a linear buckling load of about $4.0 \cdot 10^4$ N. Further details on the mesh convergence study are reported in the Appendix.

Analogously to our last work [19], we allow only the wall thickness to change during the optimizations, imposing a linear variation along the length of the CRM-like box beam defined by two design variables: the thickness at the root, $t_{\rm root}$, and the thickness at the tip, $t_{\rm tip}$. As shown in Fig. 4, the structure is divided into design segments with uniform thickness, corresponding to ribs and box sections including the stiffeners. The thickness of each patch is obtained by means of a linear interpolation between $t_{\rm root}$ and $t_{\rm tip}$ and by evaluating the thickness value at the center of each design segment.

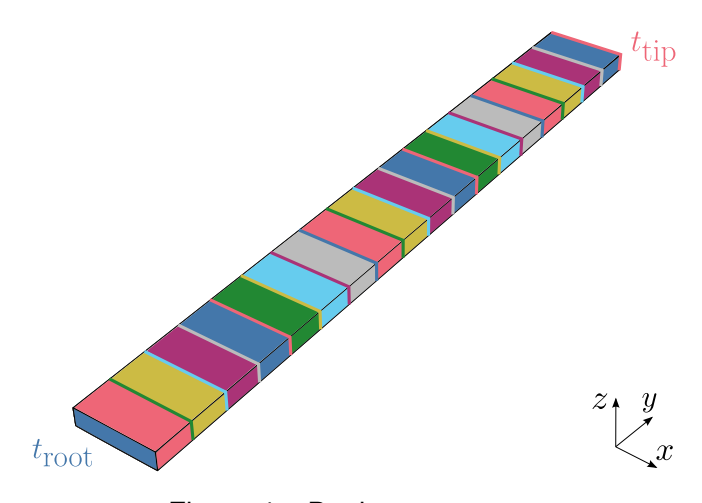


Figure 4 – Design segments.

The first optimization of the CRM-like box beam employs linear buckling constraints and serves to define a baseline structure for the optimization with nonlinear structural stability constraints. The objective is to minimize the mass of the initial CRM-like box beam while ensuring that the linear buckling load is larger than the design load and that the deformations remain elastic. All computations are performed using MSC Nastran's linear buckling solution sequence, SOL 105. The first constraint is implemented by computing the 20 smallest positive buckling load factors, representing the ratio between the buckling load and the applied load, $BLF = P_{\rm SOL\ 105}/P_{\rm design}$, and by imposing that they are all larger than 1. The second constraint is implemented by enforcing that the von Mises stress of each element is smaller than the yield strength of the material.

In summary, the optimization problem with linear buckling constraints is defined as

minimize
$$m$$
by varying $t_{\min} \leq \left[t_{\text{root}}, t_{\text{tip}}\right] \leq t_{\max}$
subject to $g_{BLF,i} = 1 - BLF_i < 0$ $i = 1, \dots, N_{BLF}$
 $g_{\sigma,j} = \sigma_j - \sigma_{\max} < 0$ $j = 1, \dots, N_e$ (7)

where t_{\min} and t_{\max} are the thickness bounds, which are set between 1 and $20\,\mathrm{mm}$, BLF_i is the *i*-th buckling load factor, with $N_{BLF}=20$, σ_j is the von Mises stress of the *j*-th element, evaluated at both the top and bottom plane of the element, and σ_{\max} is the yield strength of the material.

Instead of imposing the constraints separately on each buckling load factor and on each element, they are aggregated using Kreisselmeier-Steinhauser (KS) functions [24], such that

$$KS_{BLF} = \max_{i} \left(g_{BLF,i} \right) + \frac{1}{\rho} \ln \left(\sum_{i=1}^{N_{BLF}} \exp \left(\rho \left(g_{BLF,i} - \max_{i} \left(g_{BLF,i} \right) \right) \right) \right)$$
(8)

$$KS_{\sigma} = \max_{j} (g_{\sigma,j}) + \frac{1}{\rho} \ln \left(\sum_{j=1}^{N_e} \exp \left(\rho \left(g_{\sigma,j} - \max_{k} (g_{\sigma,j}) \right) \right) \right)$$
(9)

where ρ is the aggregation factor determining how close the KS function is to the maximum function, which is set to 100. This aggregation technique returns a single value for each constraint, representing an envelope of all the calculated quantities.

The structure obtained from the optimization with linear buckling constraints is used as starting point for the optimization with the nonlinear structural stability constraint. The latter is implemented by imposing that the 20 smallest magnitude eigenvalues of the tangent stiffness matrix are positive for all converged increments along the traced equilibrium path. The constraint on von Mises stresses is not changed, but this time nonlinear stresses are considered. A new constraint is added to this optimization, enforcing the applied load at the end of the nonlinear analysis, $P_{\rm end}$, to be equal to the design load, thus avoiding misleading the optimizer if the analysis does not converge to the prescribed load.

In summary, the optimization problem with nonlinear structural stability constraints is defined as

minimize
$$m$$
by varying $t_{\min} \leq [t_{\text{root}}, t_{\text{tip}}] \leq t_{\max}$
subject to $g_{\lambda, ij} = -\lambda_{ij} < 0$ $i = 1, \dots, N_i, \ j = 1, \dots, N_{\lambda}$
 $g_{\sigma, k} = \sigma_k - \sigma_{\max} < 0$ $k = 1, \dots, N_e$

$$g_P = 0.99 - \frac{P_{\text{end}}}{P_{\text{design}}} < 0$$
(10)

where λ_{ij} is the j-th tangent stiffness matrix eigenvalue at the i-th iteration, N_i is the number of converged increments and $N_{\lambda}=20$. The constraint on the applied load at the end of the nonlinear analysis is implemented as an inequality, where the difference with respect to the prescribed load must be smaller than 1%.

Analogously to the von Mises stresses, also the eigenvalues of the tangent stiffness matrix are aggregated using a KS function, such that

$$KS_{\lambda} = \max_{i,j} \left(g_{\lambda,ij} \right) + \frac{1}{\rho} \ln \left(\sum_{i=1}^{N_i} \sum_{j=1}^{N_{\lambda}} \exp \left(\rho \left(g_{\lambda,ij} - \max_{i,j} \left(g_{\lambda,ij} \right) \right) \right) \right). \tag{11}$$

All computations are performed using MSC Nastran's nonlinear analysis solution sequence, SOL 106. To monitor the 20 smallest magnitude eigenvalues of the tangent stiffness matrix we use a suitable DMAP invoked by the Nastran input file³.

The arc-length method is set up through the NLPARM and the NLPCI cards, whose settings are reported in Table 2. These settings are chosen with the aim of maximizing the computational efficiency of SOL 106's arc-length solver. The strategy employed consists in starting the nonlinear analysis using a relatively large arc-length increment size and then allowing the increment size to reduce in presence of nonlinearities and to increase again where the equilibrium path is mostly linear. In fact, for small applied loads the equilibrium path can be reliably followed with coarse resolution, while a fine resolution is only needed in presence of nonlinearities. The reader is referred to the *MSC Nastran Quick Reference Guide* for a detailed explanation on the meaning of the parameters.

Table 2 – Non-default parameters of the NLPARM and NLPCI Nastran cards employed for the nonlinear analyses of the CRM-like box beam.

NLPARM field	Value	NLPCI field	Value
KMETHOD	ITER	TYPE	CRIS
KSTEP	-1	MINALR	10^{-5}
MAXITER	3	DESITER	4
CONV	PU	MXINC	400
EPSU	10^{-5}		
EPSP	10^{-6}		
MAXBIS	20		

Despite being a single-discipline problem, both optimizations are set up in the OpenMDAO framework [25] in view of a future extension to a coupled aeroelastic analysis. Among the optimization algorithms available within the OpenMDAO architecture, the gradient-free COBYLA algorithm is chosen. The pyNastran library⁴ is used to interface the MSC Nastran model with the OpenMDAO framework.

4. Influence of skin curvature

4.1 Comparison of the initial structures

To investigate the influence of skin curvature on the nonlinear structural stability response and the related structural optimization, we begin by comparing the linear buckling loads of the initial structures. Figure 5 presents the buckling load factors for the curved and flat skin models. The results show that the model with flat skin has a linear buckling load that is 34% lower than that of the model with curved skin. This outcome is expected, as flat panels typically yield conservative results compared to curved ones due to their lower second moment of area.

Figure 6 illustrates the critical buckling modes of the two models. In both cases, the buckling mode involves the first rib bay of the CRM-like box beam, as viewed from the root. The figure also highlights the nodes where the maximum displacement occurs, which are coincident for the two models. For each model, the displacement along the *z*-axis of these nodes will be used to monitor the local displacement over the root obtained from the nonlinear analyses.

The nonlinear structural stability response of the initial structures is assessed by applying twice the design load to the CRM-like box beam and monitoring the displacements along the *z*-axis of the

³DMAP stands for *Direct Matrix Abstraction Program* and is a high-level language with its own compiler and grammatical rules that allows the user to modify MSC Nastran's standard solution sequences to perform custom operations. The computation employs a Lanczos algorithm to find the eigenvalues for each converged increment.

⁴https://github.com/SteveDoyle2/pyNastran, accessed May 2024.

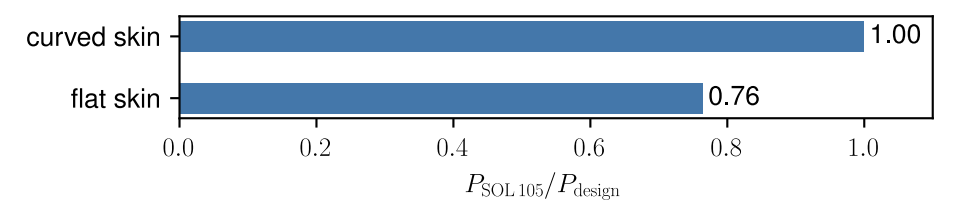


Figure 5 – Buckling load factors of the initial structures.

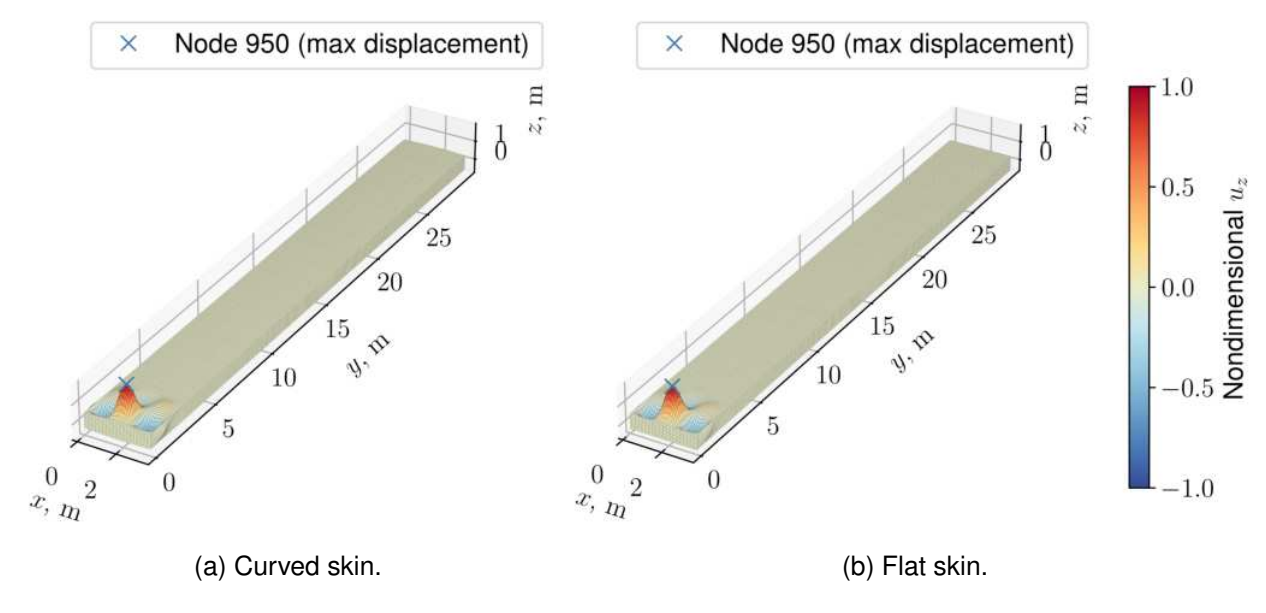


Figure 6 – Critical buckling mode of the initial structures.

nodes at the root, shown in Fig. 6, and of the nodes at the tip. Figure 7 presents this response, with the displacements nondimensionalized with respect to the width and length of the CRM-like box beam, respectively.

For the model with curved skin, the root displacement increases with the load along a stable equilibrium path until a critical point is reached. This critical point, slightly above the linear buckling load, is manifested as a load limit point. Beyond this point, the load decreases along the unstable equilibrium path until the structure reaches another load limit point, regaining stability and allowing the load to increase again. Another pair of load limit points is encountered after the displacement reaches a maximum and starts decreasing. The displacement continues to decrease until it becomes negative, after which it increases in magnitude. Finally, a last pair of closely spaced load limit points is encountered just before the displacement changes sign, though this is barely visible in the plot.

In contrast, the root displacement of the model with flat skin changes sign much earlier, approximately at the linear buckling load. The negative displacement increases in magnitude up to 0.2% of the width, where a load limit point is encountered. Along the unstable portion of the path, the displacement changes sign again and reaches a maximum at approximately $P/P_{\rm design}=1.6$, before slightly decreasing as the applied load approaches the prescribed value.

The different responses of the two models suggest the presence of a broken subcritical pitchfork bifurcation for the model with curved skin and a broken supercritical pitchfork bifurcation for the model with flat skin. The first load limit point for the curved skin model occurs without a prior large increase in displacement and at a load slightly higher than the linear buckling load. In contrast, the load limit point for the flat skin model occurs after a large increase in displacement magnitude and at a load significantly higher than the linear buckling load. These features highlight the fundamental differences between the curved and flat skin modeling approaches.

Despite the different nonlinear responses, both models show the first load limit point occurring at a higher applied load than their respective linear buckling loads. This result exemplifies the concept of the glass ceiling of linear buckling. Using a linear buckling approach, the structure would be considered able to carry only a portion of the load it can actually carry according to the nonlinear

analysis, thereby limiting the achievable mass reduction during optimization.

The equilibrium diagram of the tip displacement shows that, as expected, the model with flat skin is globally more compliant due to the smaller second moment of area. Both models exhibit a noticeable change of slope when traversing the unstable portions of their equilibrium paths.

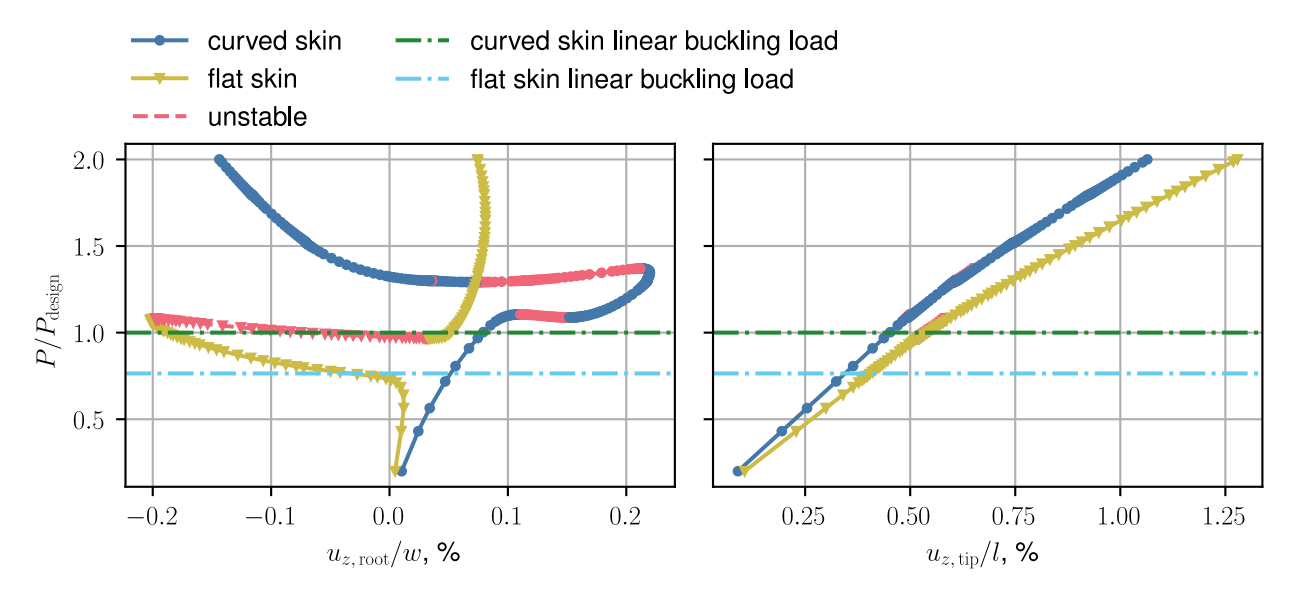


Figure 7 – Load-displacement diagram of initial structures.

Figure 8 compares the nonlinear critical load of the initial structures, corresponding to the first load limit point identified earlier along the equilibrium path of the two models. Overall, the model with flat skin results in a critical load that is 2.4% smaller than that of the model with curved skin.

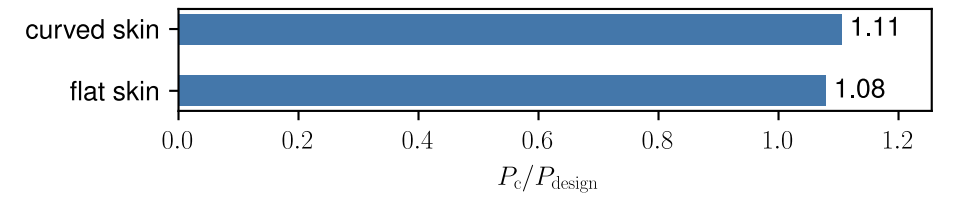


Figure 8 – Nonlinear critical loads of initial structures.

The unstable segments of the equilibrium paths shown in Fig. 7 indicate that the structure would experience snap-through when loaded past the load limit point. Figure 9 shows the deformations before and after the snap-through event for the first pair of load limit points of the model with curved skin. The snap-through event does not appear to change the number of half-waves within each ribstiffener bay, but it does exacerbate the rotations of the elements. The deformation across the second snap-through event, shown in Fig. 10, reveals a change: before the snap, a single half-wave can be observed in the central rib-stiffener bay within the first two ribs, whereas after the snap, the number of half-waves increases to two.

Figure 11 shows the deformation of the model with flat skin across the only snap-through event found in the nonlinear analysis. Here, we also observe a change in the number of half-waves within the first two ribs, however this time the change involves all three rib-stiffener bays. Furthermore, in this case the half-waves present a phase shift with respect to the model with curved skin. This finding aligns with the observation made in Fig. 7, where the unstable segments of the equilibrium paths developed towards opposite displacement directions.

4.2 Comparison of the linearly optimized structures

As described in Sec. 3, the two models are first optimized by enforcing traditional linear buckling constraints. Figure 12 shows the thickness distribution obtained from these optimizations. The optimal thickness distribution found by the optimizer for the curved skin model presents a smaller root thickness and a larger tip thickness compared to the flat skin model.

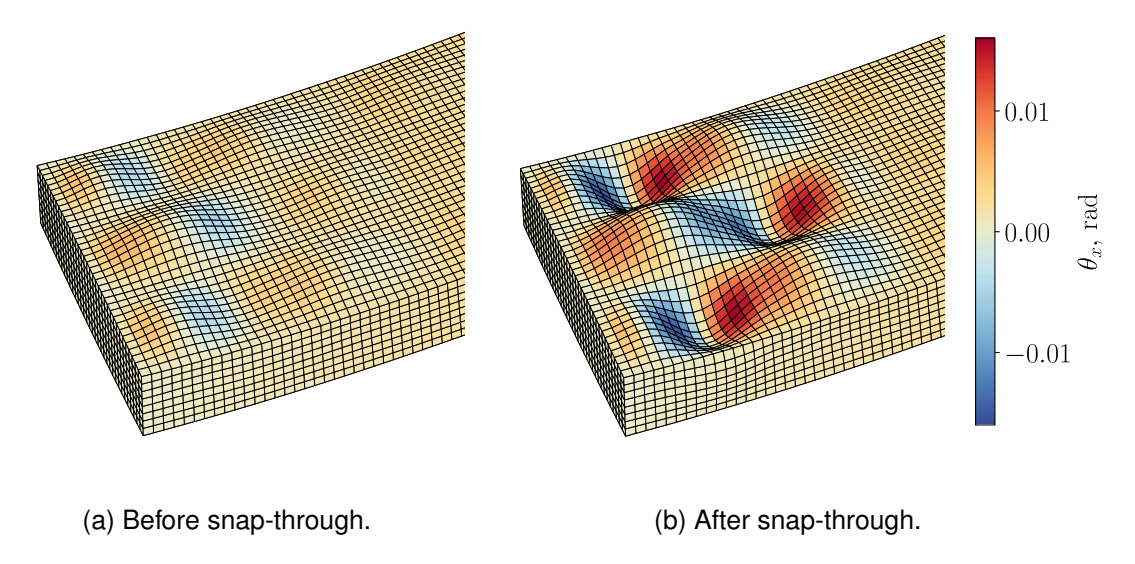


Figure 9 – Deformation over the root of the CRM-like box beam with curved skin across the first snap-through event. Displacements are amplified by a factor 60 for visualization purposes. Elements are colored by their average rotation about the *x*-axis.

Figure 13 shows the resulting mass of the two models. The model employing flat skin has a slightly larger mass, which reflects the conservatism of linear buckling approaches when considering flat skin.

Figure 14 presents the critical buckling modes of the linearly optimized structures. The model with curved skin retains a critical buckling mode similar to that of the initial structure. In contrast, the model with flat skin exhibits a completely different mode, now involving the tip of the bottom skin. Given the very small thickness of the corresponding panels and the applied load pushing these panels upward, the buckling mechanism is likely to be associated to that of the symmetric mode of a cylindrical shell under a dead load, with the curvature being provided by the bending of the bottom skin [26].

Figure 15 displays the load-displacement diagram obtained from the nonlinear analysis of the linearly optimized structures, which were loaded up to twice the design load. The root displacement of the curved skin model exhibits a broken-subcritical-pitchfork response, similar to that observed in the initial structure, with a load limit point occurring just above the linear buckling load. After regaining stability, other pairs of load limit points appear along the equilibrium path, interspersed with unstable segments. These unstable segments are not clearly visible in the plot, as they are obscured by the stable segments. These additional pair of load limit points are likely associated with the snapthrough of other rib-stiffener bays along the length of the CRM-like box beam, induced by the reduced thickness. The analysis does not converge to the prescribed load because it reaches the maximum number of allowed arc-length increments.

The model with flat skin also exhibits a response analogous to that of the initial structure, maintaining a broken-supercritical-pitchfork response. Despite the smaller mass of the linearly optimized curved skin model, the tip displacement plot indicates that it maintains a stiffer global response compared to the flat skin model. This larger global stiffness can be ascribed to the larger second moment of area of the cross-sectional geometry.

The nonlinear critical loads of the two linearly optimized structures are illustrated in Fig. 16. It can be observed that the critical load of the model with flat skin is substantially larger than that of the model with curved skin. This finding suggests a reversal of the situation observed in the analysis of the initial structures, with the use of flat skin now resulting in a larger margin between the linear buckling load and the nonlinear critical load compared to the curved skin model. This outcome indicates that employing flat skin for nonlinear stability assessments may be non-conservative, as it suggests an overly optimistic margin for mass reduction compared to the more realistic curved skin model.

Finally, Fig. 17 shows the nonlinear deformation at the design load of the two linearly optimized structures, with the elements colored according to their average rotation about the *x*-axis. As expected, no evident buckling-like deformation pattern is visible over the top skin of either model. Instead, some

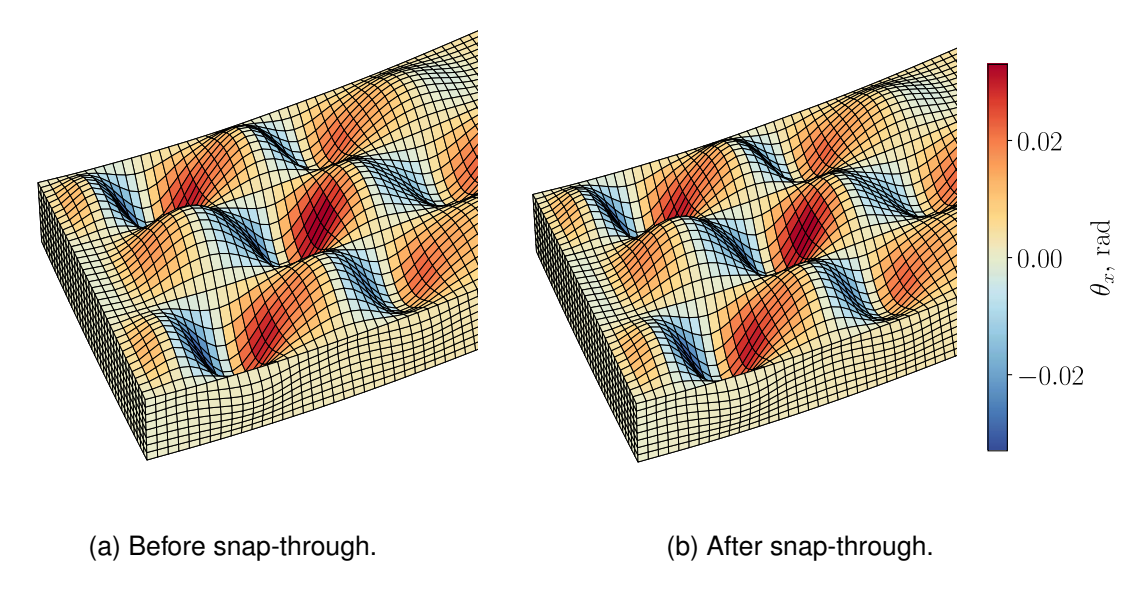


Figure 10 – Deformation over the root of the CRM-like box beam with curved skin across the second snap-through event. Displacements are amplified by a factor 60 for visualization purposes. Elements are colored by their average rotation about the *x*-axis.

local rotations are increasingly evident towards the tip, especially for the flat skin model, caused by the applied load pulling the skin upwards in the areas immediately next to the ribs.

4.3 Comparison of the nonlinearly optimized structures

The linearly optimized structures serve as the baseline for subsequent optimizations incorporating nonlinear structural stability constraints, resulting in the thickness distributions depicted in Fig. 18. The thickness distributions of the two models are now more similar if compared to those of the linearly optimized structures. Notably, the curved skin model exhibits slightly larger root and tip thicknesses than the flat skin model. In fact, Fig. 19 indicates that the curved skin model achieves a higher final mass compared to the flat skin model. Relative to the linearly optimized structures, the curved skin model sees only a 3.1% mass reduction, while the flat skin model achieves a 9.3% reduction.

This outcome is consistent with the earlier finding that the linearly optimized flat skin model possesses a greater nonlinear structural stability margin than its curved skin counterpart. Consequently, this result suggests that, for the current case study, modeling the wingbox skin as flat surfaces should be avoided in nonlinear structural stability assessments. Such an approach can result in non-conservative estimates of the critical stability load, leading to overly optimistic mass reductions. Figure 20 shows the load-displacement diagrams of the nonlinearly optimized structures, together with their linear buckling loads. The responses of the two models remain analogous to those of the initial structures. Specifically, the curved skin model still exhibits a broken-subcritical-pitchfork type of response, and the flat skin model still exhibits a broken-supercritical-pitchfork type of response. It can be noted that in both cases the optimizer has placed the design load just below the nonlinear critical load. The curved skin model results in a slightly smaller linear buckling load, at about 72% of the design load, while the linear buckling load of the flat skin model is approximately 73% of the design load.

The critical buckling modes corresponding to the linear buckling load of the nonlinearly optimized structures are depicted in Fig. 21. In contrast to the results from the linear buckling optimization, the curved skin model now exhibits a critical buckling mode involving the tip of the bottom skin. Meanwhile, the flat skin model demonstrates a critical buckling mode similar to that of the initial structure. This change in the buckling mode of the curved skin model is attributed to a more significant decrease in tip thickness compared to root thickness. Conversely, in the flat skin model, only the root thickness decreases while the tip thickness remains at the lower bound of 1 mm.

Finally, the deformation of the nonlinearly optimized structures at the design load is shown in Fig. 22. A buckling-like pattern can be observed over the top skin of the flat skin model, which is absent in the curved skin model. These different deformation patterns reflect the distinct nature of the nonlinear

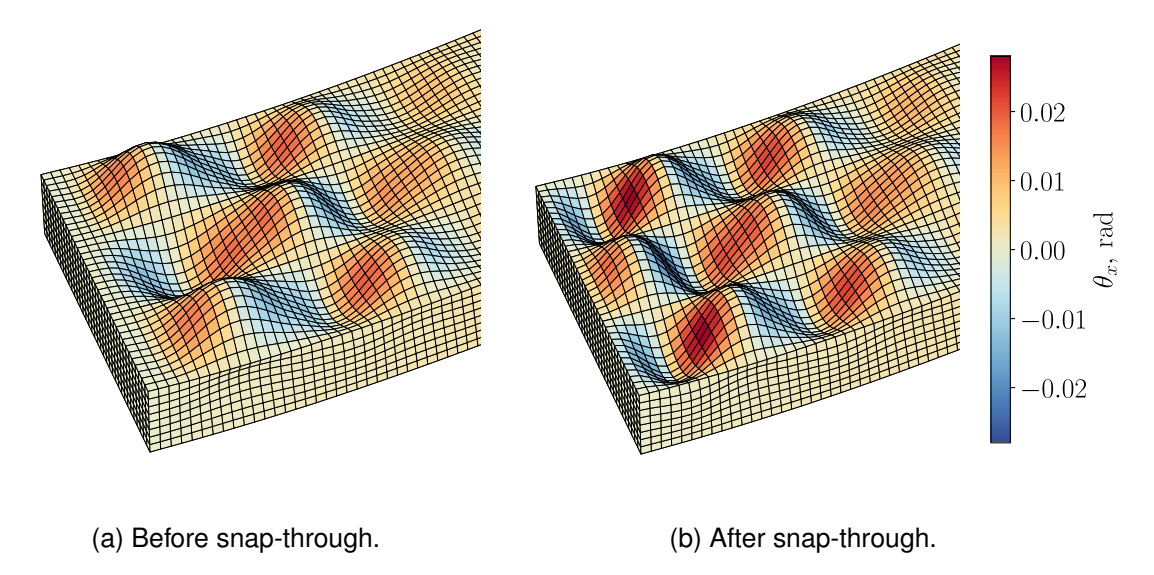


Figure 11 – Deformation over the root of the CRM-like box beam with flat skin across the snap-through event. Displacements are amplified by a factor 60 for visualization purposes. Elements are colored by their average rotation about the *x*-axis.

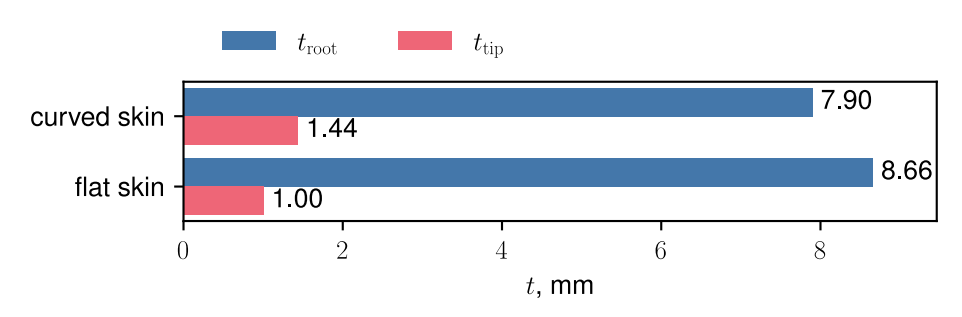


Figure 12 – Thickness distribution of the linearly optimized structures.

responses of the two models. The broken-subcritical-pitchfork type of response does not produce large local rotations before the load limit point, whereas the broken-supercritical-pitchfork type of response is responsible for the emergence of the buckling-like pattern before the load limit point. This result further underscores the importance of accurately modeling the curvature of the skin when assessing the nonlinear stability of a wingbox structure.

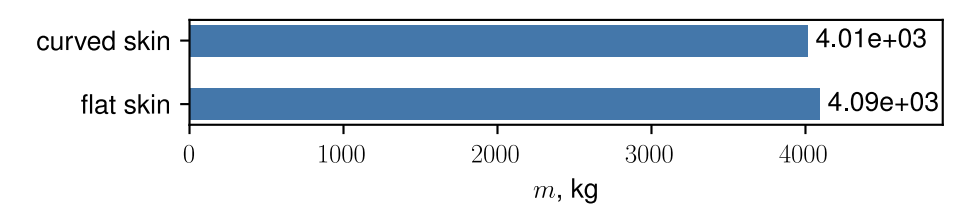


Figure 13 – Mass of the linearly optimized structures.

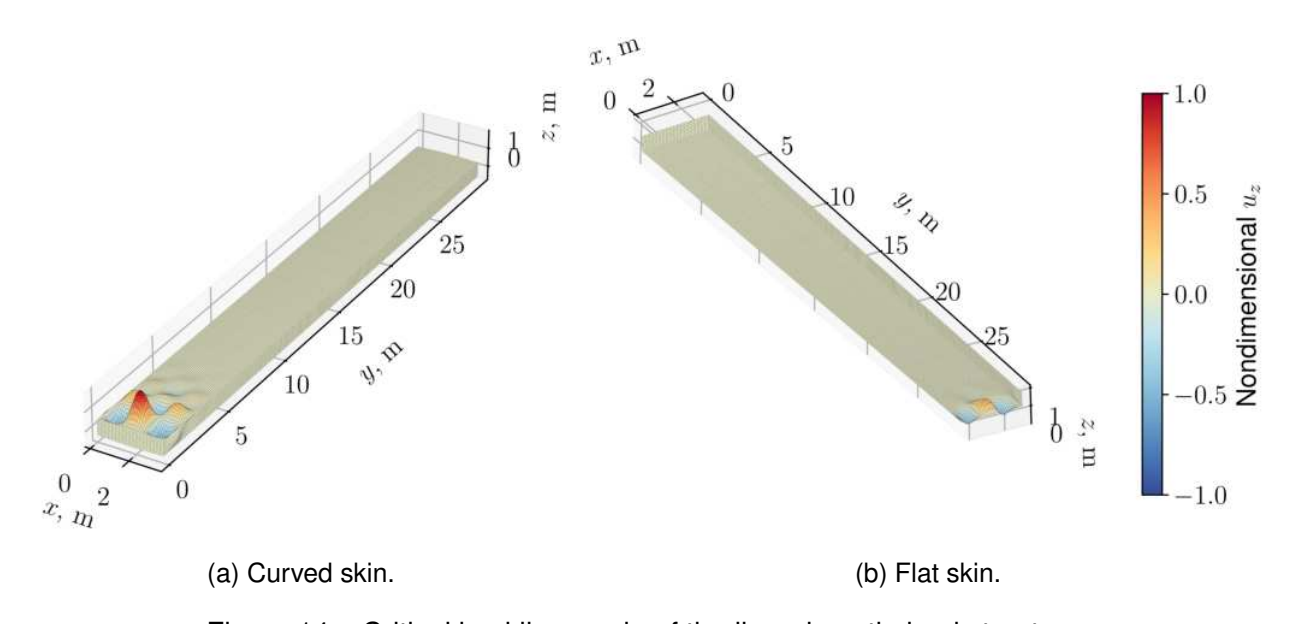


Figure 14 – Critical buckling mode of the linearly optimized structures.

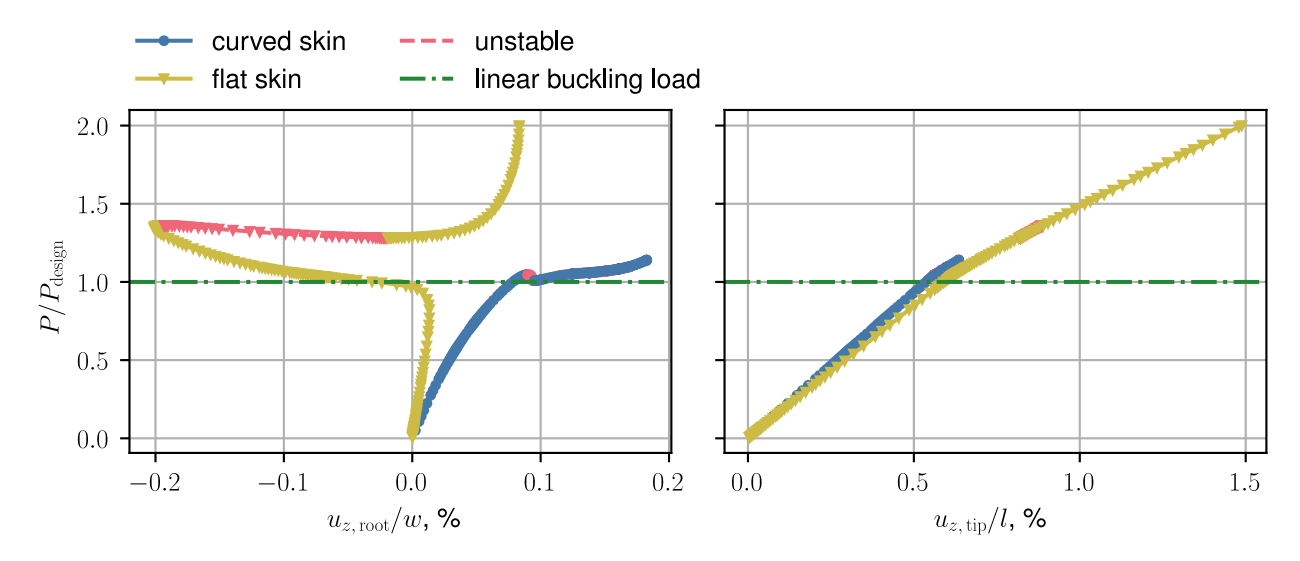


Figure 15 – Load-displacement diagram of the linearly optimized structures.

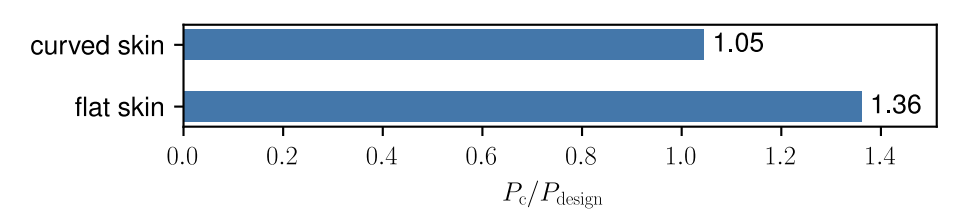


Figure 16 – Nonlinear critical loads of linearly optimized structures.

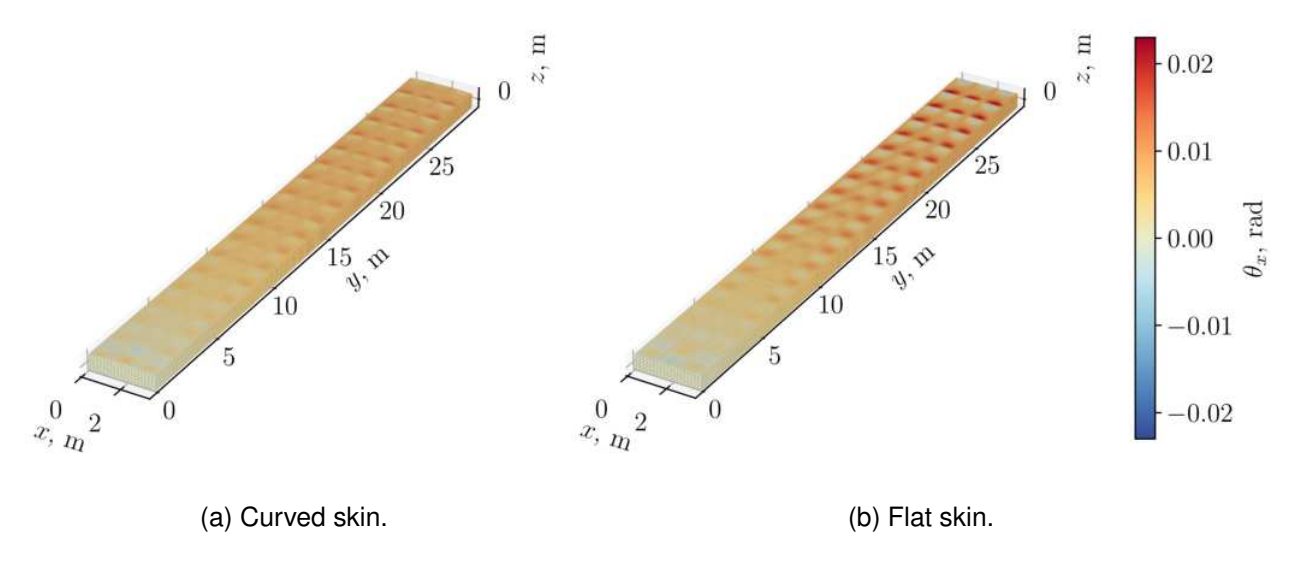


Figure 17 – Deformation at design load of the linearly optimized structures.

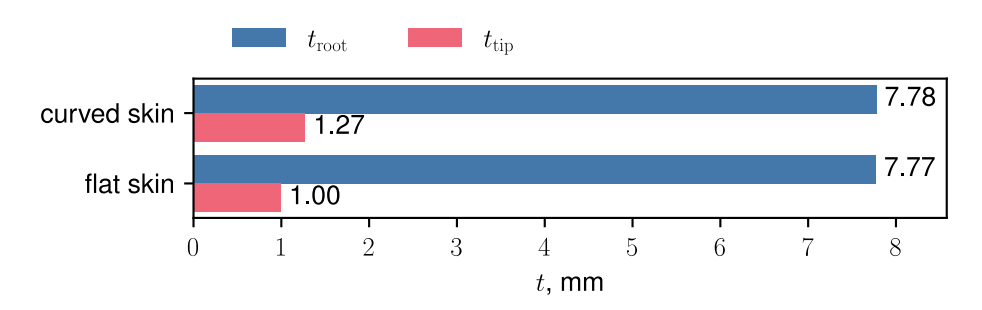


Figure 18 – Thickness distribution of the nonlinearly optimized structures.

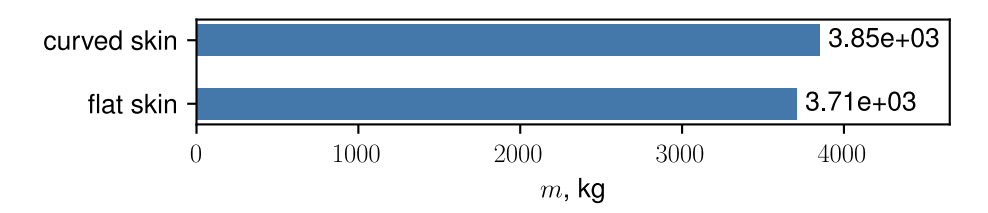


Figure 19 – Mass of the nonlinearly optimized structures.

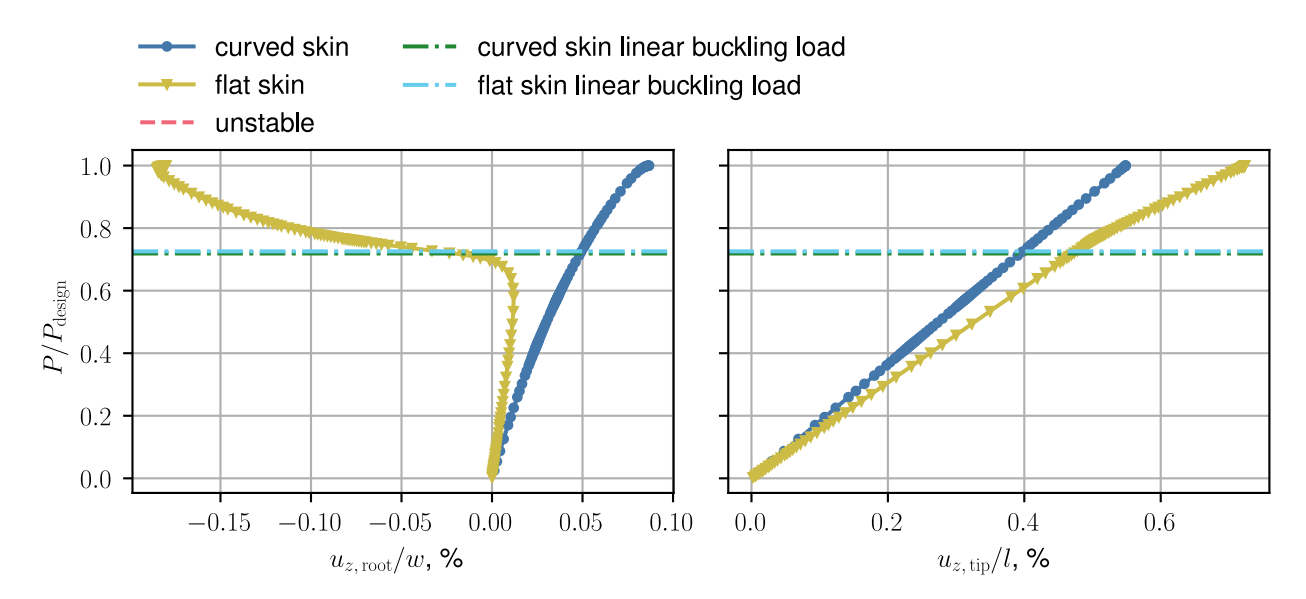


Figure 20 – Load-displacement diagram of the nonlinearly optimized structures.

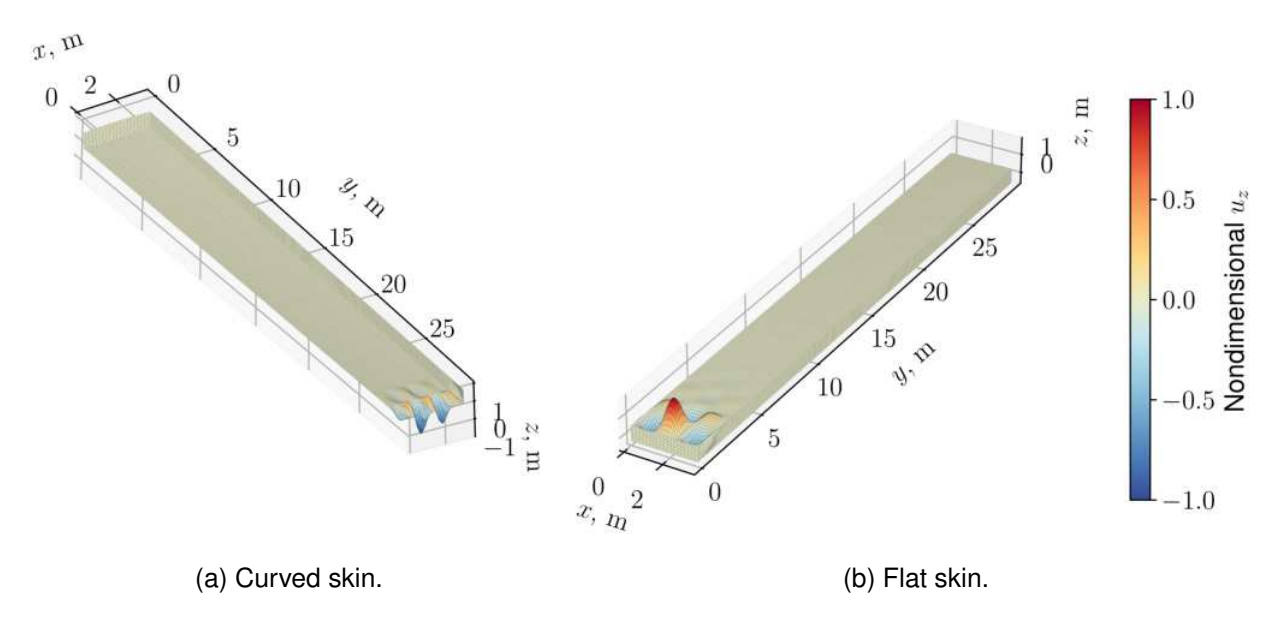


Figure 21 – Critical buckling mode of the nonlinearly optimized structures.

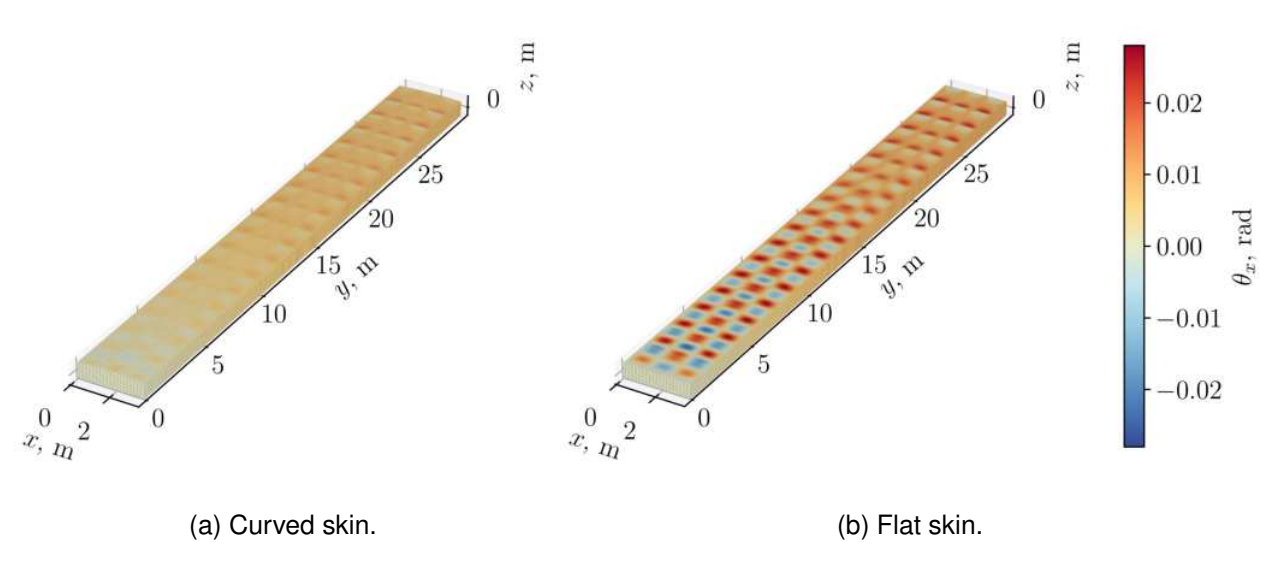


Figure 22 – Deformation at design load of the nonlinearly optimized structures.

5. Conclusion

This study examined the impact of skin curvature on the analysis and optimization of an idealized wingbox using nonlinear structural stability constraints. The investigation compared two versions of the CRM-like box beam model: one with curved skin and another with flat skin. The study involved an initial optimization with traditional linear buckling constraints, followed by a subsequent optimization with nonlinear structural stability constraints.

The linear buckling analysis of the initial structures revealed that the flat skin model exhibited a 34% lower buckling load compared to the curved skin model, which was anticipated due to the lower second moment of area provided by the flat panels. The nonlinear analysis demonstrated that the flat skin model's stability response was characterized by a broken supercritical pitchfork bifurcation, while the curved skin model displayed a broken subcritical pitchfork bifurcation.

Linear buckling optimizations resulted in a marginally higher mass for the flat skin model compared to the curved skin model, confirming the conservativeness of using flat panels in linear stability methods. The nonlinear analysis of the linearly optimized structures showed that the flat skin model had a higher nonlinear critical load than the curved skin model. This suggests that, contrary to typical linear stability results, using flat skin may lead to non-conservative nonlinear stability estimations.

The subsequent nonlinear structural stability optimizations further supported this indication, as the curved skin model ended up with slightly larger root and tip thicknesses, leading to a higher mass. The nonlinear response trends observed in the initial models persisted in the optimized structures, with the flat skin model exhibiting a broken-supercritical-pitchfork response and the curved skin model showing a broken-subcritical-pitchfork response.

Finally, the deformation patterns of the nonlinearly optimized structures at the design load highlighted the differences in their nonlinear behavior. The top skin of the flat skin model displayed a buckling-like pattern, which was absent in the curved skin model, emphasizing the importance of accurately modeling skin curvature in structural stability assessments.

In conclusion, this study underscores the critical importance of considering skin curvature in the development of aeroelastic optimizations that implement nonlinear structural stability constraints. The findings suggest that modeling wingbox skin as flat panels can lead to non-conservative estimates of the nonlinear critical stability load, potentially resulting in overly optimistic mass reductions. Therefore, for more accurate and reliable optimization outcomes, it is imperative to incorporate realistic skin curvatures in structural models.

Future work will focus on extending this approach to fully-coupled aeroelastic optimization frameworks, incorporating more complex loading conditions, and investigating more realistic wingbox layouts to further validate the findings presented in this paper.

6. Contact Author Email Address

fma.mitrotta@bristol.ac.uk

7. Copyright Statement

The authors confirm that they, and/or their company or organization, hold copyright on all of the original material included in this paper. The authors also confirm that they have obtained permission, from the copyright holder of any third party material included in this paper, to publish it as part of their paper. The authors confirm that they give permission, or have obtained permission from the copyright holder of this paper, for the publication and distribution of this paper as part of the ICAS proceedings or as individual off-prints from the proceedings.

Appendix

A mesh convergence study is performed by running the MSC Nastran linear buckling solution sequence, SOL 105, on the model with curved skin applying a load $P=1\,\mathrm{N}$. Increasing mesh resolutions are considered and the predicted linear buckling load, $P_{\mathrm{SOL}\ 105}$, is monitored. The results of the mesh convergence study are shown in Fig. 23. The mesh is defined to be converged when the difference of the linear buckling load with respect to the one obtained with the finest mesh is below 1%

Since the mesh convergence study is executed with the use of linear buckling analyses, the convergence of the mesh is verified in the nonlinear regime. To do this, two nonlinear analyses are

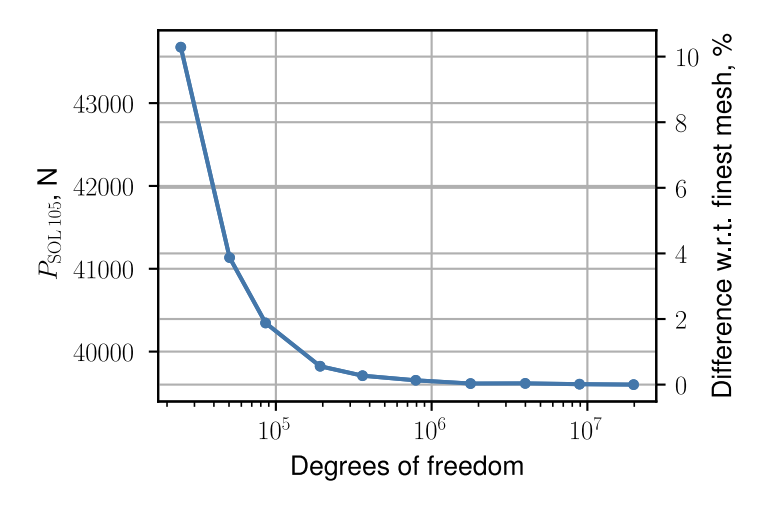


Figure 23 – Mesh convergence study of the CRM-like box beam model with curved skin.

performed, one using the original mesh resulting from the convergence study and another one using a refined mesh generated by choosing a target element length equal to half the element length used for the original mesh. The applied load is set to twice the linear buckling load obtained for the original mesh to capture the nonlinear region of the structural response.

The results of these analyses are shown in Fig. 24 in terms of a 3D load-displacement diagram combining the local displacement at the root, the tip displacement, and the applied load. The local displacement at the root is evaluated for both models at the node where each linear buckling analysis predicts the maximum displacement for the critical buckling mode. For the model employing the original mesh, this node is shown in Fig. 6a, and its position is analogous for the model employing the refined mesh.

It can be observed that the two analyses predict the same behavior for the entirety of the equilibrium path. The load of the first limit point of the model employing the original mesh is only 0.7% higher than the corresponding load of the model employing the refined mesh. This result suggests that the original mesh is detailed enough to capture the part of the nonlinear response of the CRM-like box beam that is of interest for the optimization studies.

The histories of the optimizations performed for this paper are shown in Figs. from 25 to 28. Since the COBYLA algorithm does not always end the optimization on a design point satisfying all the constraints, the results shown in this paper are always related to the last feasible design point.

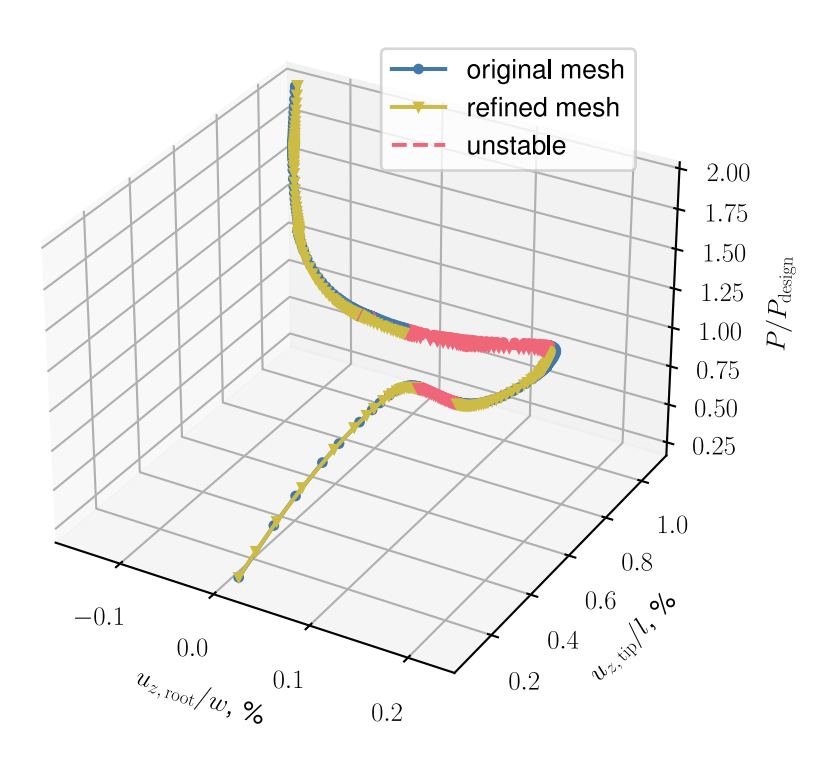


Figure 24 – Load-displacement equilibrium paths obtained with the original and the refined mesh of the CRM-like box beam.

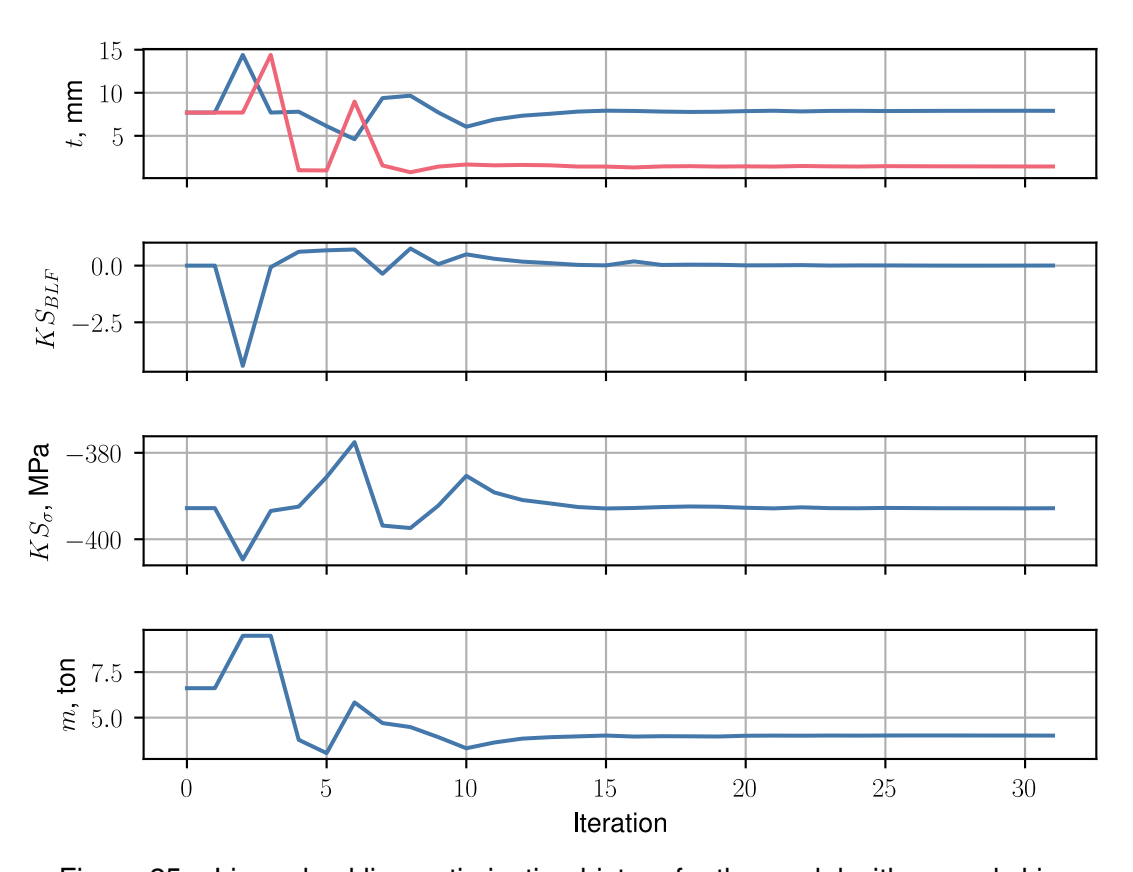


Figure 25 – Linear buckling optimization history for the model with curved skin.

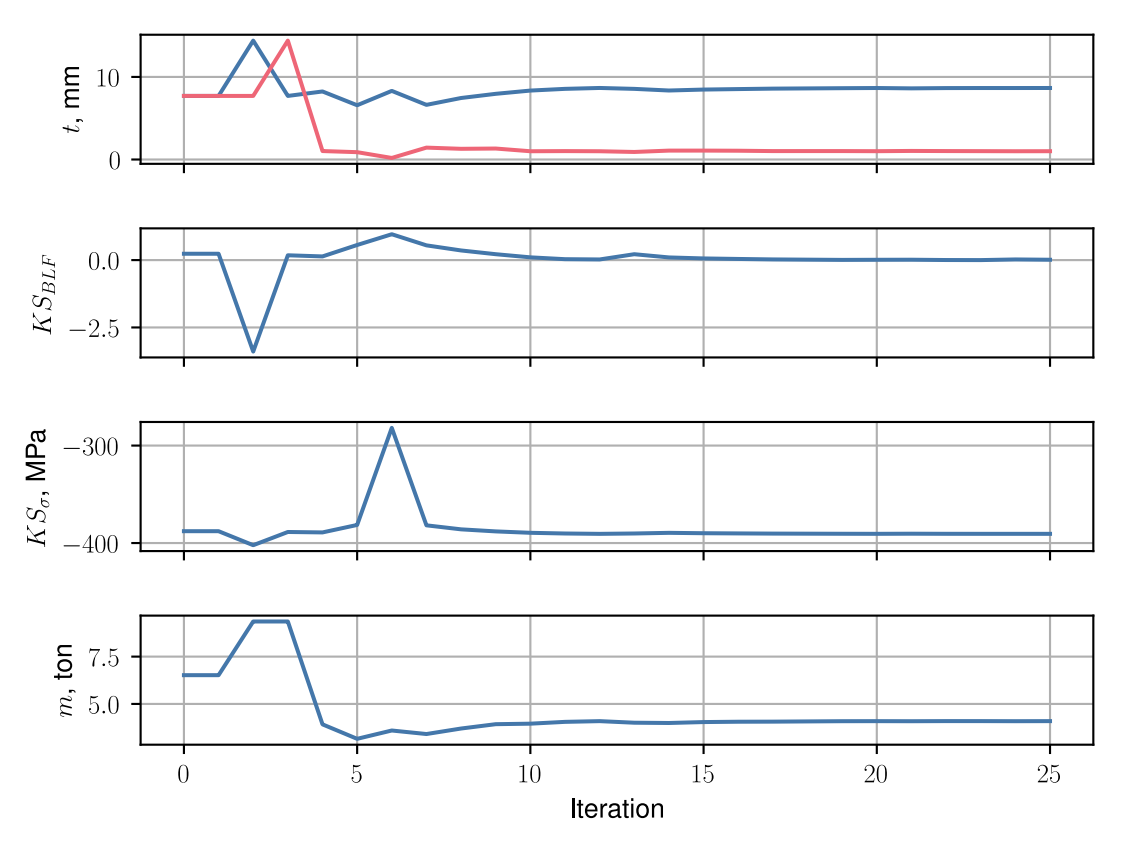


Figure 26 – Linear buckling optimization history for the model with flat skin.

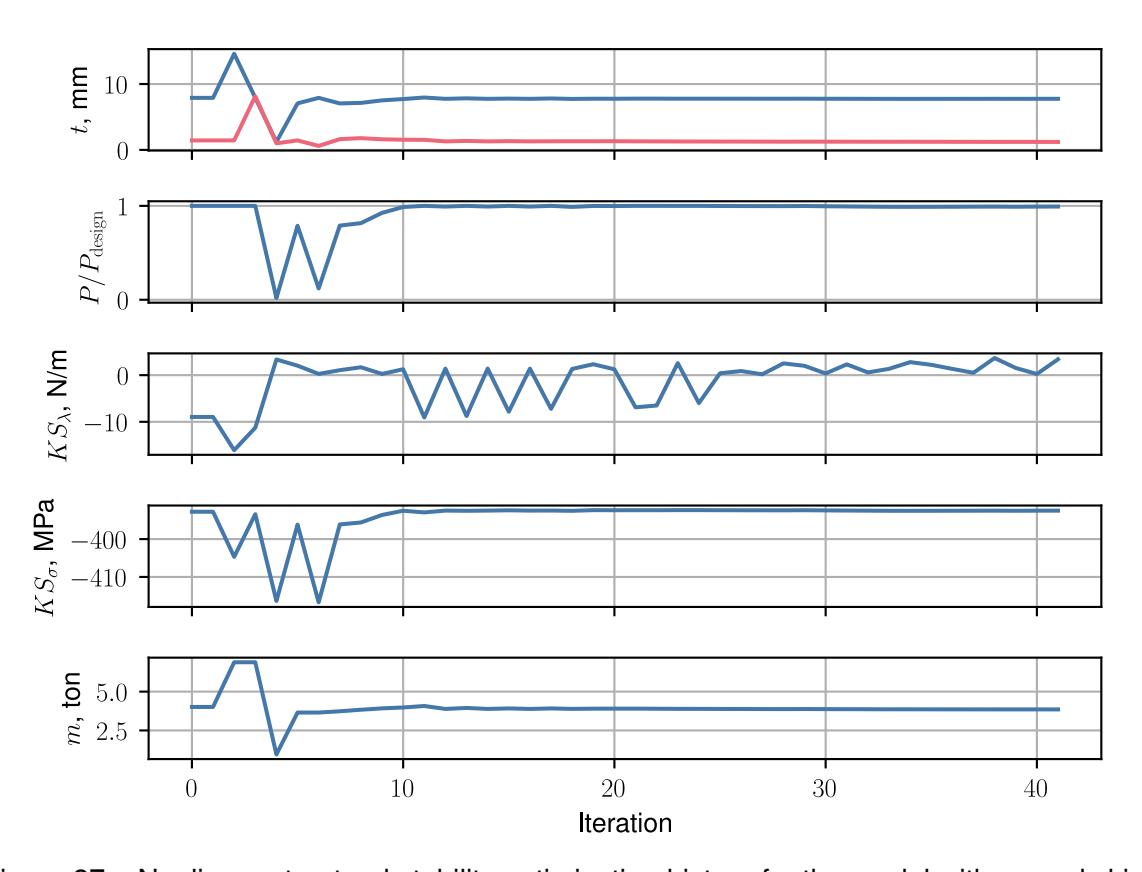


Figure 27 – Nonlinear structural stability optimization history for the model with curved skin.

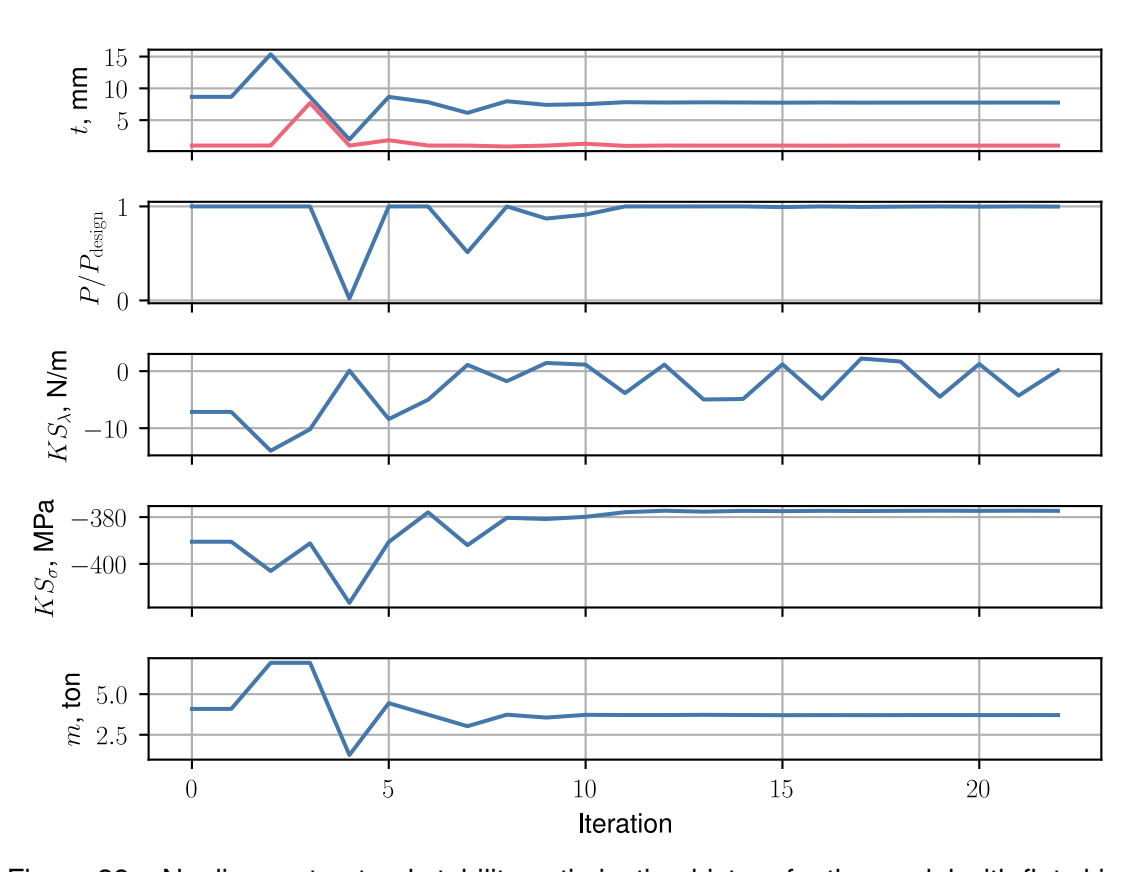


Figure 28 – Nonlinear structural stability optimization history for the model with flat skin.

Acknowledgments

This research was supported by Embraer S.A. and by the Engineering and Physical Sciences Research Council (EPSRC) via grant EP/T517872/1. The authors would like to thank Mike Coleman from Hexagon for his contribution to the development of the DMAP program for the calculation of the eigenvalues of the tangent stiffness matrix.

References

- [1] Commitment to Fly Net Zero. https://aviationbenefits.org/flynetzero/, 2021. Accessed November 2023.
- [2] A Filippone. Flight Performance of Fixed and Rotary Wing Aircraft. Elsevier, 2006.
- [3] J. K. S. Dillinger, T. Klimmek, M. M. Abdalla, and Z. Gürdal. Stiffness optimization of composite wings with aeroelastic constraints. *Journal of Aircraft*, 50(4):1159–1168, 2013.
- [4] Bret K. Stanford, Christine V. Jutte, and Carol D. Wieseman. Trim and structural optimization of subsonic transport wings using nonconventional aeroelastic tailoring. *AIAA Journal*, 54(1):293–309, 2016.
- [5] O. Stodieck, J. E. Cooper, P. M. Weaver, and P. Kealy. Aeroelastic tailoring of a representative wing box using tow-steered composites. *AIAA Journal*, 55(4):1425–1439, 2017.
- [6] Bret K. Stanford and Christine V. Jutte. Comparison of curvilinear stiffeners and tow steered composites for aeroelastic tailoring of aircraft wings. *Computers & Structures*, 183:48–60, 2017.
- [7] Muhammad F. Othman, Gustavo H.C. Silva, Pedro H. Cabral, Alex P. Prado, Alberto Pirrera, and Jonathan E. Cooper. A robust and reliability-based aeroelastic tailoring framework for composite aircraft wings. *Composite Structures*, 208:101–113, 2019.
- [8] Shuvodeep De, Mohamed Jrad, and Rakesh K. Kapania. Structural optimization of internal structure of aircraft wings with curvilinear spars and ribs. *Journal of Aircraft*, 56(2):707–718, 2019.
- [9] Timothy R. Brooks, Joaquim R.R.A. Martins, and Graeme J. Kennedy. High-fidelity aerostructural optimization of tow-steered composite wings. *Journal of Fluids and Structures*, 88:122–147, 2019.
- [10] Eduardo P. Krupa, Jonathan E. Cooper, Alberto Pirrera, and Raj Nangia. Improved aerostructural performance via aeroservoelastic tailoring of a composite wing. *The Aeronautical Journal*, 122(1255):1442–1474, 2018.
- [11] Gustavo H. C. Silva, Alex Pereira do Prado, Pedro Higino Cabral, Roeland De Breuker, and Johannes K. S. Dillinger. Tailoring of a composite regional jet wing using the slice and swap method. *Journal of Aircraft*, 56(3):990–1004, 2019.
- [12] D. Rajpal, E. Gillebaart, and R. De Breuker. Preliminary aeroelastic design of composite wings subjected to critical gust loads. *Aerospace Science and Technology*, 85:96–112, 2019.
- [13] Marco Tito Bordogna, Paul Lancelot, Dimitri Bettebghor, and Roeland De Breuker. Static and dynamic aeroelastic tailoring with composite blending and manoeuvre load alleviation. *Structural and Multidisci-plinary Optimization*, 61(5):2193–2216, May 2020.
- [14] Timothy R. Brooks and Benjamin D. Smith. *Aerostructural design optimization of the D8 aircraft using active aeroelastic tailoring*. 2020.
- [15] Alasdair C. Gray and Joaquim R. Martins. *Geometrically Nonlinear High-fidelity Aerostructural Optimization for Highly Flexible Wings.* 2021.
- [16] C. Niu. Airframe Structural Design: Practical Design Information and Data on Aircraft Structures. Conmilit Press, 1988.
- [17] Francesco M. A. Mitrotta, Alberto. Pirrera, Macquart. Terence, Jonathan E. Cooper, Alex Pereira do Prado, and Pedro Higino Cabral. Proof of concept of a nonlinear structural stability constraint for aeroelastic optimization. *The Aeronautical Journal*, 2023, submitted.
- [18] John Vassberg, Mark Dehaan, Melissa Rivers, and Richard Wahls. *Development of a Common Research Model for Applied CFD Validation Studies*. 2008.
- [19] Francesco Mario Antonio Mitrotta, Alberto Pirrera, Terence Macquart, Jonathan E. Cooper, Alex Pereira do Prado, and Pedro Higino Cabral. On the influence of load introduction method on wingbox optimization with nonlinear structural stability constraints. In *International Forum on Aeroelasticity and Structural Dynamics*, pages 2024–031, 2024.
- [20] Zdeněk P Bažant and Luigi Cedolin. Stability of Structures. WORLD SCIENTIFIC, 2010.
- [21] Sofie E. Leon, Glaucio H. Paulino, Anderson Pereira, Ivan F. M. Menezes, and Eduardo N. Lages. A Unified Library of Nonlinear Solution Schemes. *Applied Mechanics Reviews*, 64(4), 08 2012. 040803.
- [22] Jeffrey D. Taylor and Douglas F. Hunsaker. *Characterization of the Common Research Model Wing for Low-Fidelity Aerostructural Analysis*. 2021.

- [23] Timothy R. Brooks, Gaetan K. W. Kenway, and Joaquim R. R. A. Martins. Benchmark aerostructural models for the study of transonic aircraft wings. *AIAA Journal*, 56(7):2840–2855, 2018.
- [24] Joaquim R. R. A. Martins and Andrew Ning. *Engineering Design Optimization*. Cambridge University Press, Jan 2022.
- [25] Justin S. Gray, John T. Hwang, Joaquim R. R. A. Martins, Kenneth T. Moore, and Bret A. Naylor. Open-MDAO: An Open-Source Framework for Multidisciplinary Design, Analysis, and Optimization. *Structural and Multidisciplinary Optimization*, 59:1075–1104, 2019.
- [26] R.M.J. Groh and A. Pirrera. Orthotropy as a driver for complex stability phenomena in cylindrical shell structures. *Composite Structures*, 198:63–72, 2018.